











ARTICLE

<https://doi.org/10.1038/s41467-019-10392-w>

OPEN

# Isolated single atom cobalt in Bi<sub>3</sub>O<sub>4</sub>Br atomic layers to trigger efficient CO<sub>2</sub> photoreduction

Jun Di <sup>1,6</sup>, Chao Chen <sup>1,6</sup>, Shi-Ze Yang <sup>4</sup>, Shuangming Chen<sup>3</sup>, Meilin Duan <sup>3</sup>, Jun Xiong<sup>2</sup>, Chao Zhu<sup>1</sup>, Ran Long <sup>3</sup>, Wei Hao<sup>1</sup>, Zhen Chi<sup>5</sup>, Hailong Chen <sup>5</sup>, Yu-Xiang Weng <sup>5</sup>, Jiexiang Xia<sup>2</sup>, Li Song <sup>3</sup>, Shuzhou Li <sup>1</sup>, Huaming Li<sup>2</sup> & Zheng Liu <sup>1</sup>

The design of efficient and stable photocatalysts for robust CO<sub>2</sub> reduction without sacrifice reagent or extra photosensitizer is still challenging. Herein, a single-atom catalyst of isolated single atom cobalt incorporated into Bi<sub>3</sub>O<sub>4</sub>Br atomic layers is successfully prepared. The cobalt single atoms in the Bi<sub>3</sub>O<sub>4</sub>Br favors the charge transition, carrier separation, CO<sub>2</sub> adsorption and activation. It can lower the CO<sub>2</sub> activation energy barrier through stabilizing the COOH\* intermediates and tune the rate-limiting step from the formation of adsorbed intermediate COOH\* to be CO\* desorption. Taking advantage of cobalt single atoms and two-dimensional ultrathin Bi<sub>3</sub>O<sub>4</sub>Br atomic layers, the optimized catalyst can perform light-driven CO<sub>2</sub> reduction with a selective CO formation rate of 107.1 μmol g<sup>-1</sup> h<sup>-1</sup>, roughly 4 and 32 times higher than that of atomic layer Bi<sub>3</sub>O<sub>4</sub>Br and bulk Bi<sub>3</sub>O<sub>4</sub>Br, respectively.

<sup>1</sup>Center for Programmable Materials, School of Materials Science & Engineering, Nanyang Technological University, Singapore 639798, Singapore. <sup>2</sup>School of Chemistry and Chemical Engineering, Institute for Energy Research, Jiangsu University, 301 Xuefu Road, Zhenjiang 212013, China. <sup>3</sup>National Synchrotron Radiation Laboratory, CAS Center for Excellence in Nanoscience, School of Chemistry and Materials Science, University of Science and Technology of China, Hefei, Anhui 230029, China. <sup>4</sup>Materials Science and Technology Division, Oak Ridge National Laboratory, Oak Ridge 37830, USA. <sup>5</sup>Laboratory of Soft Matter Physics, Institute of Physics, Chinese Academy of Sciences, Beijing 100190, China. <sup>6</sup>These authors contributed equally: Jun Di, Chao Chen. Correspondence and requests for materials should be addressed to J.X. (email: [xjx@ujs.edu.cn](mailto:xjx@ujs.edu.cn)) or to L.S. (email: [song2012@ustc.edu.cn](mailto:song2012@ustc.edu.cn)) or to Z.L. (email: [z.liu@ntu.edu.sg](mailto:z.liu@ntu.edu.sg))

Photocatalytic CO<sub>2</sub> reduction with water as reaction medium to yield value-added carbon products has been regarded as an appealing approach to remit the energy issue and manage the global carbon balance simultaneously<sup>1–5</sup>. Despite a good deal of impressive photocatalysts have been developed for CO<sub>2</sub> reduction, most of them are still subjected to low photocatalytic activity, poor product selectivity or the requirement of sacrificial agent, which greatly limit the possible practical applications. Hence, it is desirable to design robust catalysts with high reduction efficiency, high selectivity without the utilization of sacrifice reagent.

Recently, ultrathin two-dimensional (2D) materials with suitable energy band structure have been demonstrated distinct advantages as one class of emerging photocatalysts<sup>6–10</sup>. The atomic thickness with concomitant huge specific surface area allows better absorption of ultraviolet-visible light. The ultrathin configuration can significantly decrease the bulk recombination possibility of charge carriers owing to the shortened diffusion distance from inside to surface. Moreover, the high ratio of coordination-unsaturated surface atoms to overall atoms can afford more sites facilitating the interfacial reactions<sup>11</sup>. Especially, the single species of surface atoms is conducive to the production of highly selective CO<sub>2</sub> reduction products<sup>12–14</sup>. Up to now, several types of ultrathin nanosheets have been developed and employed for CO<sub>2</sub> photoreduction, such as WO<sub>3</sub> layers<sup>12</sup>, ultrathin ZnAl LDH<sup>13</sup>, single-unit-cell o-BiVO<sub>4</sub><sup>14</sup>, Bi<sub>2</sub>WO<sub>6</sub> layers<sup>15</sup>, and one-unit-cell ZnIn<sub>2</sub>S<sub>4</sub><sup>16</sup>. However, the high surface charge recombination rate and lack of active sites limits the sufficient utilization of charge carriers to trigger the photoreduction process. In order to further improve the CO<sub>2</sub> reduction efficiency, incorporating isolated single atoms into 2D ultrathin nanosheets may be an appealing strategy. With maximum atom-utilization efficiency and unique properties, single-atom catalysts (SAC) display enormous potential in different catalytic applications<sup>17,18</sup>. Considering the cobalt (Co) SAC show outstanding performance toward electrocatalytic CO<sub>2</sub> reduction due to the unique electronic structure, it is desirable to introduce Co single atoms as active sites to build Co SA/2D materials and employed for CO<sub>2</sub> photoreduction<sup>19,20</sup>. Moreover, this allocation affords a favorable platform to in-depth insight the structure–property relationship between doped single atoms and the corresponding photocatalytic activity. Herein, taking the ultrathin Bi<sub>3</sub>O<sub>4</sub>Br nanosheets as a prototype, isolated single-atom Co is incorporated into Bi<sub>3</sub>O<sub>4</sub>Br atomic layers to build a Co–Bi<sub>3</sub>O<sub>4</sub>Br catalyst and employed for CO<sub>2</sub> photoreduction.

## Results

**Characterizations of Co–Bi<sub>3</sub>O<sub>4</sub>Br nanosheets.** X-ray diffraction (XRD) and Raman spectra suggest the successful preparation of orthorhombic Bi<sub>3</sub>O<sub>4</sub>Br and the Co incorporation did not destroy the crystal structure (Supplementary Fig. 1). The transmission electron microscopy (TEM) image in Supplementary Fig. 2a–c depicts a sheet-like morphology of Bi<sub>3</sub>O<sub>4</sub>Br with the thickness of 1.89 nm, corresponding to unit cell (*c* parameter) thickness of Bi<sub>3</sub>O<sub>4</sub>Br. The observed lattice spacing of 0.285 nm is corresponded to the (020) or (200) crystal plane spacing of Bi<sub>3</sub>O<sub>4</sub>Br, revealing the (002) facet exposure (Supplementary Fig. 2d). The TEM and atomic force microscope images of Co–Bi<sub>3</sub>O<sub>4</sub>Br-1 show the similar morphology and thickness with pure Bi<sub>3</sub>O<sub>4</sub>Br (Fig. 1a, b, Supplementary Fig. 3). To disclose the fine structure and distribution of Co, atomic resolution high-angle annular dark-field scanning TEM (HAADF-STEM) is performed. The isolated dark dots Fig. 1c, d can be unambiguously ascribed to individual Co atoms according to the Z-contrast difference between the light Co and the heavier Bi atoms<sup>21</sup>. The isolated Co atoms are

substituting Bi atoms in the crystal lattice. In addition, elemental mapping with subnanometer resolution (Fig. 1e, f) shows a uniform, uncorrelated spatial distribution of Co with a content of 0.8 wt%.

To further disclose the Co coordination environment, X-ray absorption near-edge structure and extended X-ray absorption fine structure (EXAFS) spectroscopy are performed. The difference in position and intensity of pre-edge peak at about 7711 eV signify that the Co atoms in the samples are of diverse environments (Fig. 2a)<sup>22</sup>. The Co K-edge absorption edge position of Co–Bi<sub>3</sub>O<sub>4</sub>Br-1 is located close to CoO rather than Co foil, suggesting single Co atom carries positive charge with the valence state is approach +2. The Bi L<sub>3</sub>-edge absorption edge position of Co–Bi<sub>3</sub>O<sub>4</sub>Br-1 shows slight difference with that of Bi<sub>3</sub>O<sub>4</sub>Br, suggesting distinct local atomic structure due to Co incorporation (Fig. 2b). View from the Fourier transformed (FT) k<sup>3</sup>-weighted EXAFS spectra (Fig. 2c), Co–Bi<sub>3</sub>O<sub>4</sub>Br-1 materials does not emerge the peak of Co–Co bond in reference to standard Co foil and CoO, revealing the absence of Co or CoO clusters/particles. These results demonstrate that the Co species are isolated single atoms. The main peak at 1.49 Å for Co–Bi<sub>3</sub>O<sub>4</sub>Br-1 is corresponding to the coordination with O atoms in Bi<sub>3</sub>O<sub>4</sub>Br lattice<sup>22</sup>. Beyond that, the main peak at around 1.5 Å in Bi L<sub>3</sub>-edge EXAFS spectra is assigned to the Bi–O bonds, in which the intensity of Co–Bi<sub>3</sub>O<sub>4</sub>Br-1 is weaker than that of Bi<sub>3</sub>O<sub>4</sub>Br (Fig. 2d)<sup>23</sup>. All these result qualitatively verify their distinct local atomic arrangement of Co–Bi<sub>3</sub>O<sub>4</sub>Br-1 relative to the Bi<sub>3</sub>O<sub>4</sub>Br, also certified by the peak shifting in X-ray photoelectron spectra (XPS, Supplementary Fig. 4) and decreased zeta potentials from 29.9 mV for Bi<sub>3</sub>O<sub>4</sub>Br to 18.4 mV for Co–Bi<sub>3</sub>O<sub>4</sub>Br-1 (Supplementary Fig. 5).

**Photocatalytic CO<sub>2</sub> reduction performances.** The photocatalytic CO<sub>2</sub> reduction performance of the samples is examined in neutral water under simulated solar light irradiation without any sacrificial reagents or photosensitizers. As shown in Fig. 3a, the Bi<sub>3</sub>O<sub>4</sub>Br atomic layer displays a CO formation rate of 27.0 μmol g<sup>−1</sup> h<sup>−1</sup>, greatly higher than the 3.3 μmol g<sup>−1</sup> h<sup>−1</sup> for bulk Bi<sub>3</sub>O<sub>4</sub>Br (Supplementary Fig. 6), revealing the advantage of 2D ultrathin configuration. After the isolated single-atom Co is incorporated into Bi<sub>3</sub>O<sub>4</sub>Br atomic layers, the photocatalytic activity can be further improved. Among the diverse Co–Bi<sub>3</sub>O<sub>4</sub>Br materials, the Co–Bi<sub>3</sub>O<sub>4</sub>Br-1 displays the optimal performance. During a 20 h photocatalysis test, the total yield of CO can arrive 2142.1 μmol g<sup>−1</sup>, accompanied by a trace amount of methane (~3.28 μmol g<sup>−1</sup>). The average CO-generation rate of Co–Bi<sub>3</sub>O<sub>4</sub>Br-1 is up to 107.1 μmol g<sup>−1</sup> h<sup>−1</sup>, roughly 4 and 32 times higher than that of Bi<sub>3</sub>O<sub>4</sub>Br atomic layer and bulk Bi<sub>3</sub>O<sub>4</sub>Br, respectively. This value is also higher than many ultrathin materials under the same testing conditions (Supplementary Fig. 7) and superior to many reported results (Supplementary Table 1). During the photoreduction process, Co–Bi<sub>3</sub>O<sub>4</sub>Br-1 sample can simultaneously achieve H<sub>2</sub>O oxidation into O<sub>2</sub> with an average O<sub>2</sub> evolution rates of about 56 μmol g<sup>−1</sup> h<sup>−1</sup> (Supplementary Fig. 8). The ratio of CO evolution rates to O<sub>2</sub> evolution rates is 1.91, approach to the stoichiometric ratio of 2. Through tune the different usage amount of photocatalyst for CO<sub>2</sub> reduction, the higher converted value of μmol g<sup>−1</sup> h<sup>−1</sup> can be achieved when less usage amount is employed (Supplementary Fig. 9). The control experiments in dark, under Ar condition or without catalyst did not show the evolution of CO, implying the CO is indeed produced by CO<sub>2</sub> photoreduction. The <sup>13</sup>CO<sub>2</sub> isotopic labeling experiment is performed, in which the peak at *m/z* = 29 (<sup>13</sup>CO) can be observed, further affirming the formation of CO is indeed derived from the reduction of CO<sub>2</sub> (Fig. 3b). Furthermore, the apparent quantum yields for Co–Bi<sub>3</sub>O<sub>4</sub>Br-1 are calculated

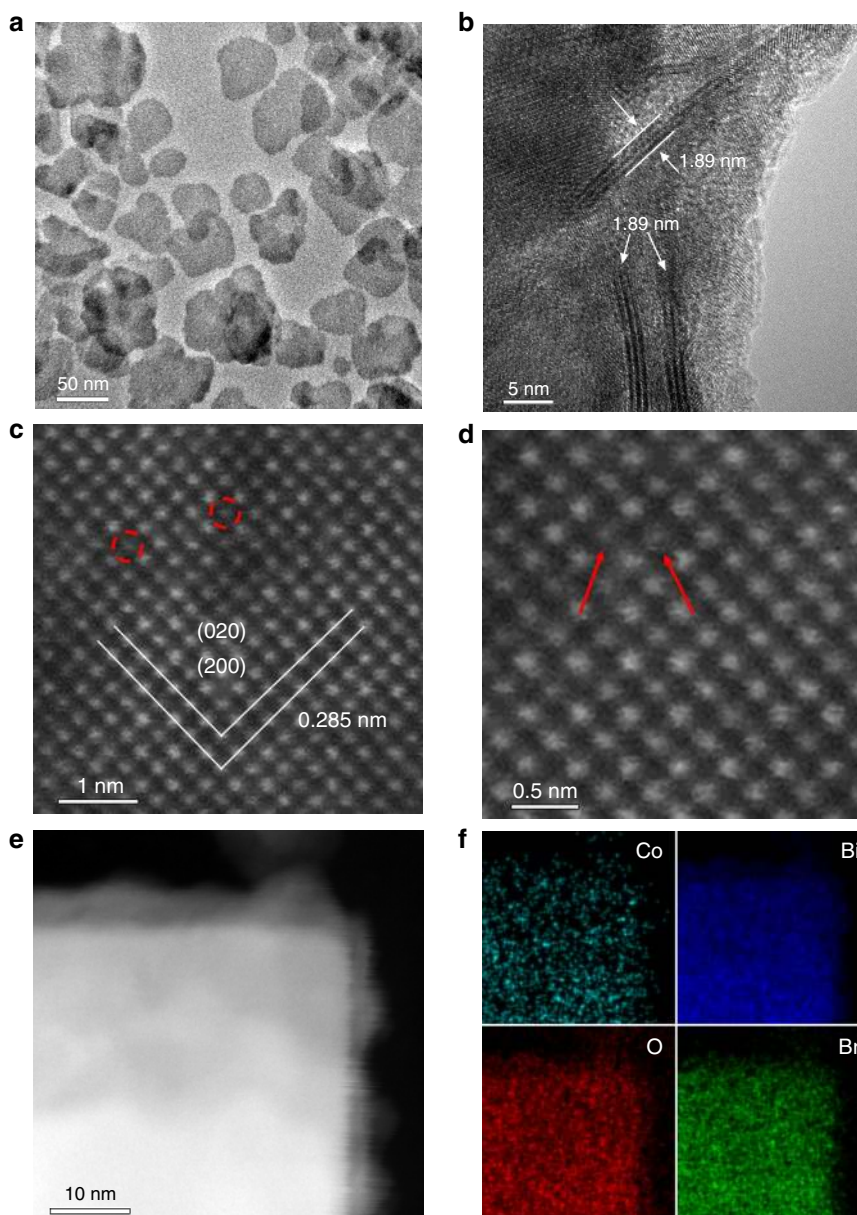


**Fig. 1** Surface morphology of Co-Bi<sub>3</sub>O<sub>4</sub>Br-1. **a, b** TEM and **c, d** atomic resolution HAADF-STEM images of Co-Bi<sub>3</sub>O<sub>4</sub>Br-1, **e, f** STEM image and EDS mapping images of Co, Bi, O, and Br

to be approximately 0.91% and 0.36% at 380 and 400 nm, respectively. To determine the stability, the XRD, XPS valence-band spectra and TEM are employed for the used Co-Bi<sub>3</sub>O<sub>4</sub>Br-1 samples (Supplementary Fig. 10). No obvious variations of the crystal structure, electronic structure and morphology can be observed after the photoreaction, suggesting the favorable photostability.

**Insight of the increased photocatalytic activity.** To elucidate the origin of the increased photocatalytic activity, three elementary processes in photocatalytic CO<sub>2</sub> reduction namely light absorption, charge separation, and interfacial CO<sub>2</sub> catalysis are taken into consideration<sup>24</sup>. After the incorporation of single-atom Co, the absorption in the visible light area can be improved due to the formed dopant energy levels of Co in the bandgap of Bi<sub>3</sub>O<sub>4</sub>Br (Supplementary Fig. 11a). The electrons in the valence band (VB) can be excited to the newly formed localized state of high-spin Co<sup>2+</sup> (3d<sup>7</sup>). Moreover, the fully occupied electrons in t<sub>2</sub> levels of Co<sup>2+</sup> can be easily excited to the unoccupied e levels

(d-d internal transitions), also contribute to the improved light absorption<sup>25</sup>. The increased density of states of Co-Bi<sub>3</sub>O<sub>4</sub>Br in the bandgap through density functional theory (DFT) calculation further confirm the easily transition of photogenerated electrons to the new energy levels (Supplementary Fig. 11c, d). The corresponding bandgap energy of Bi<sub>3</sub>O<sub>4</sub>Br and Co-Bi<sub>3</sub>O<sub>4</sub>Br-1 are calculated to be 2.29 and 2.21 eV, respectively (Supplementary Fig. 11b). The detailed energy-level positions of VB edges determined from XPS VB spectra are both 1.06 eV (Supplementary Fig. 11e). Thus, the conduction band (CB) potentials of Bi<sub>3</sub>O<sub>4</sub>Br and Co-Bi<sub>3</sub>O<sub>4</sub>Br-1 are determined to be -1.23 and -1.15 eV, respectively, satisfying the thermodynamic requirements for CO<sub>2</sub> reduction to yield CO (Supplementary Fig. 11f).

To study the dynamic behaviors of photogenerated charge carriers in the prepared samples, ultrafast transient absorption (TA) spectra is employed. The biexponential fitting results are  $\tau_1 = 12$  ps and  $\tau_2 = 400$  ps for Bi<sub>3</sub>O<sub>4</sub>Br, while  $\tau_1 = 11$  ps and  $\tau_2 = 1$  ns for Co-Bi<sub>3</sub>O<sub>4</sub>Br-1 (Fig. 3c). Interestingly, the isolated

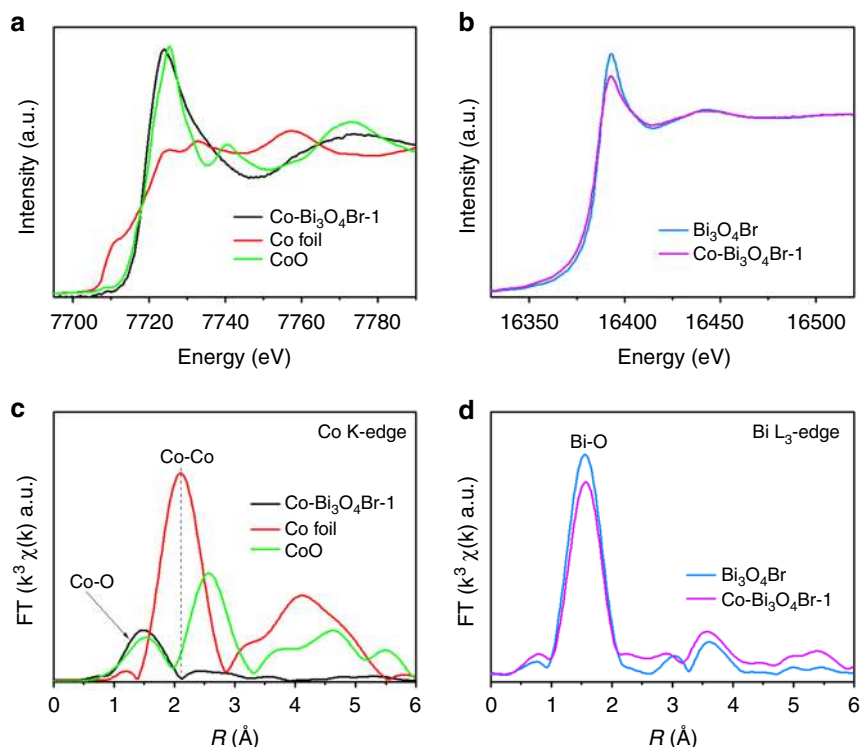


**Fig. 2** Synchrotron radiation XAFS measurements. **a** Co K-edge XANES spectra, **b** Bi L<sub>3</sub>-edge XANES spectra, EXAFS spectra of **c** Co K-edge and **d** Bi L<sub>3</sub>-edge

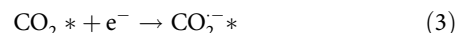
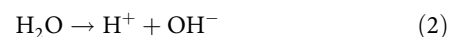
single-atom Co nearly not alter  $\tau_1$ , but endows a  $\sim 2.5$ -fold increase for  $\tau_2$ . The  $\tau_1$  corresponded to electrons capture from CB into trap states within the bandgap, while the much slower decay component  $\tau_2$  represents the recombination between the trapped electrons and the VB holes<sup>16</sup>. The engineered isolated single-atom Co can supply trap states to capture more photogenerated electrons, while the more long-lived, trapped electrons afford more opportunities for CO<sub>2</sub> photoreduction. Moreover, time-resolved fluorescence emission decay spectra and surface photovoltage (SPV) spectroscopy are employed for further exploration (Supplementary Fig. 12a, b). The average fluorescence lifetime and SPV intensity of Co-Bi<sub>3</sub>O<sub>4</sub>Br-1 are much higher than that of Bi<sub>3</sub>O<sub>4</sub>Br atomic layers, respectively, further suggesting the increased charge separation efficiency in Co-Bi<sub>3</sub>O<sub>4</sub>Br. The isolated single-atom Co can work as charge separation center to trap the photogenerated electrons<sup>26,27</sup>, and thus increase the carrier utilization efficiency toward redox reactions, also certified by the transient photocurrent responses and electrochemical impedance spectroscopy (Supplementary Fig. 12c, d).

To dive deep into the interfacial catalysis of CO<sub>2</sub> to yield CO, CO<sub>2</sub> surface adsorption, activation, and CO desorption processes are explored. Firstly, the CO<sub>2</sub> adsorption is generally considered as a prerequisite for CO<sub>2</sub> photoreduction reaction. The isolated single-atom Co<sup>2+</sup> by replacing Bi<sup>3+</sup> enables the Co-Bi<sub>3</sub>O<sub>4</sub>Br atomic layers to be more negatively charged, which may in favor of CO<sub>2</sub> adsorption on the surfaces<sup>16</sup>. It can be testified by the increased CO<sub>2</sub> adsorption capacity of Co-Bi<sub>3</sub>O<sub>4</sub>Br-1 relative to Bi<sub>3</sub>O<sub>4</sub>Br, as illustrated in Fig. 3d. Contact-angle measurement demonstrates that hydrophilicity may be not the crucial factor to affect CO<sub>2</sub> photoreduction reaction (Supplementary Fig. 13). Subsequently, the in situ Fourier transform infrared spectroscopy (FTIR) measurements are carried out to acquire in-depth understanding on the reaction intermediates (Fig. 3e). The peaks at 1256, 1337, and 1508 cm<sup>-1</sup> can be assigned to CO<sub>2</sub><sup>-</sup>, symmetric

O-C-O stretches of b-CO<sub>3</sub><sup>2-</sup> and m-CO<sub>3</sub><sup>2-</sup> groups, respectively<sup>28,29</sup>. Notably the gradually increased peak at 1567 cm<sup>-1</sup> is ascribed to COOH\* intermediate, a type of critical intermediate during the formation of CO<sub>2</sub> to CO<sup>6,29</sup>. The band at  $\sim 1600$  cm<sup>-1</sup> in the dark 30 min line is ascribed to the asymmetric O-C-O stretch of b-CO<sub>3</sub><sup>2-</sup> groups. With the prolonged light irradiation time, this band is obscured by the significantly increased COOH\* band. Lastly, the CO desorption is also considered as an important factor to decide the entirely photocatalysis efficiency. As shown from CO temperature-programmed desorption (TPD), the Co-Bi<sub>3</sub>O<sub>4</sub>Br-1 exhibits lower onset desorption temperature and higher overall amount of detected CO, revealing the formed CO\* molecules can liberate from the Co-Bi<sub>3</sub>O<sub>4</sub>Br-1 surface much easier (Fig. 3f)<sup>28</sup>. In addition, compared to the Bi<sub>3</sub>O<sub>4</sub>Br, a new lower-temperature desorption peak around 518 °C can be observed, implying the incorporated Co single atoms may favor the CO desorption, and this result is also certified by the calculated desorption free energy of CO (Fig. 4b).

## Discussion

According to the analysis, the possible CO<sub>2</sub> reduction mechanism can be summarized as follows (Fig. 4a, Supplementary Fig. 14):



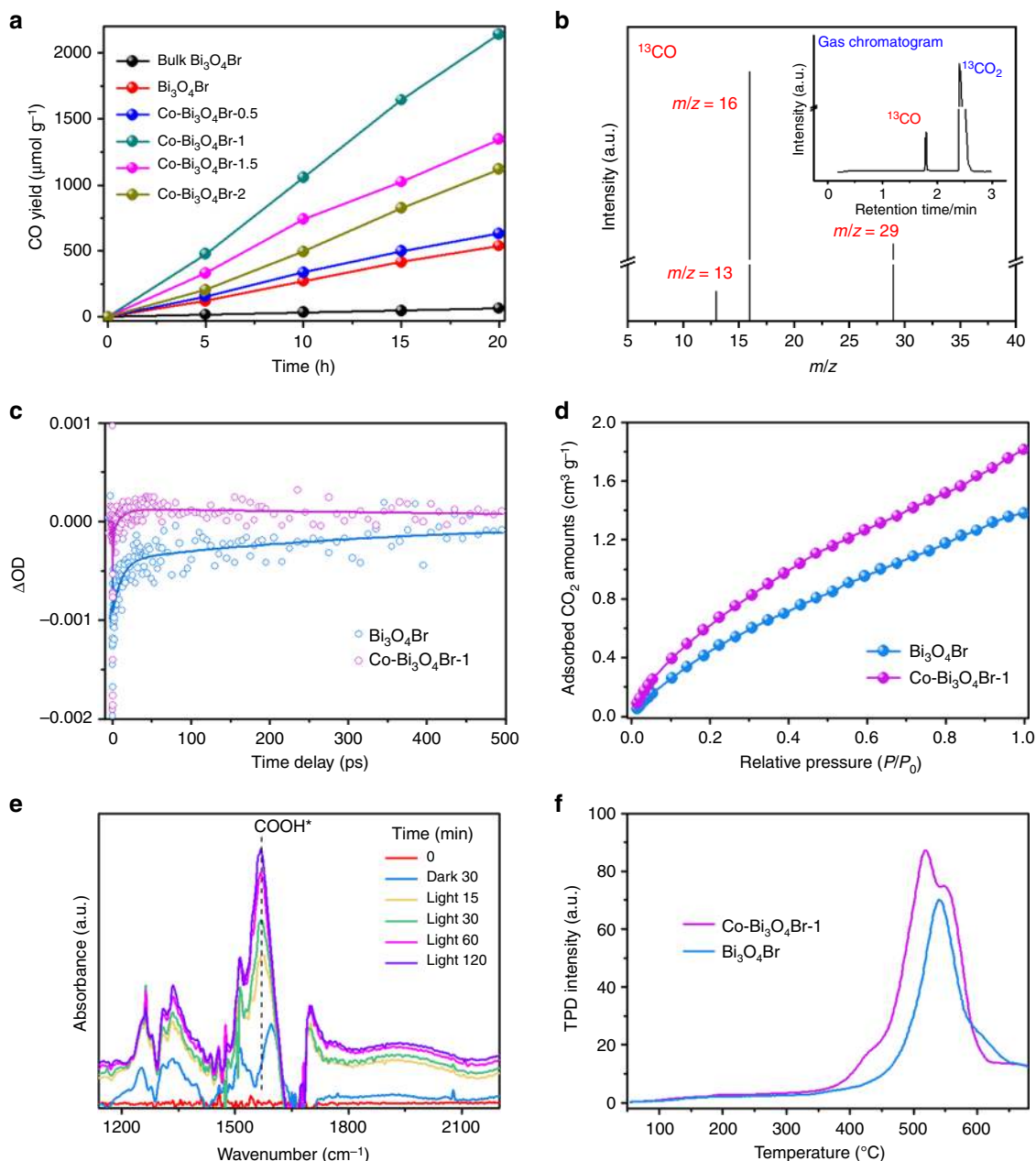


**Fig. 3** Evaluation of CO<sub>2</sub> photoreduction performance and mechanism insight. **a** Photoreduction of CO<sub>2</sub> into CO over Bi<sub>3</sub>O<sub>4</sub>Br and Co-Bi<sub>3</sub>O<sub>4</sub>Br materials, **b** mass spectra of <sup>13</sup>CO ( $m/z = 29$ ) produced over Co-Bi<sub>3</sub>O<sub>4</sub>Br-1 in photoreduction of <sup>13</sup>CO<sub>2</sub>, **c** ultrafast TA spectra of Bi<sub>3</sub>O<sub>4</sub>Br and Co-Bi<sub>3</sub>O<sub>4</sub>Br, **d** CO<sub>2</sub> adsorption isotherms of Bi<sub>3</sub>O<sub>4</sub>Br and Co-Bi<sub>3</sub>O<sub>4</sub>Br-1, **e** in situ FTIR spectra for the CO<sub>2</sub> reduction process on the Co-Bi<sub>3</sub>O<sub>4</sub>Br-1, **f** CO TPD spectra of Bi<sub>3</sub>O<sub>4</sub>Br and Co-Bi<sub>3</sub>O<sub>4</sub>Br-1

where “\*” on behalf of the adsorption state at the materials surface.

The CO<sub>2</sub> molecules are adsorbed on the surface of catalysts and the H<sub>2</sub>O molecules are dissociated into hydroxyl and hydrogen ions. The CO<sub>2</sub>\* will be preferential combine with electron and hydrogen ion to form a carboxyl radical and then disintegrated into the adsorbed CO\*<sup>30</sup>. Eventually, the adsorbed CO\* will desorb from the catalyst surface to form gaseous CO.

To explore the reactivity nature and CO<sub>2</sub> catalytic reduction cycle, DFT calculations are carried out (Fig. 4). Both the formation of COOH\* and desorption of CO\* for the Bi<sub>3</sub>O<sub>4</sub>Br are highly endergonic processes. The formation of adsorbed intermediate COOH\* is found as the potential limiting step (Fig. 4b). However, the incorporated Co in Bi<sub>3</sub>O<sub>4</sub>Br can lower the CO<sub>2</sub>

activation energy barrier through stabilizing the COOH\* intermediates and tuning the rate-limiting step to be CO\* desorption.

In conclusion, isolated single-atom Co are incorporated into the Bi<sub>3</sub>O<sub>4</sub>Br atomic layers to generate photocatalysts with superior activity for CO<sub>2</sub> reduction. Benefiting from the cooperation of ultrathin configuration and isolated single-atom Co, the Co-Bi<sub>3</sub>O<sub>4</sub>Br exhibits excellent photocatalytic activity toward CO<sub>2</sub> reduction to high selective yield CO, with a high formation rate of 107.1 μmol g<sup>-1</sup> h<sup>-1</sup>, roughly 4 and 32 times higher than that of Bi<sub>3</sub>O<sub>4</sub>Br atomic layer and bulk Bi<sub>3</sub>O<sub>4</sub>Br, respectively. The Co single atoms in the Bi<sub>3</sub>O<sub>4</sub>Br benefit the charge transition, charge-carrier separation kinetics, CO<sub>2</sub> adsorption and activation. It can lower the CO<sub>2</sub> activation energy barrier through stabilizing the COOH\* intermediates and tunes the rate-limiting step from

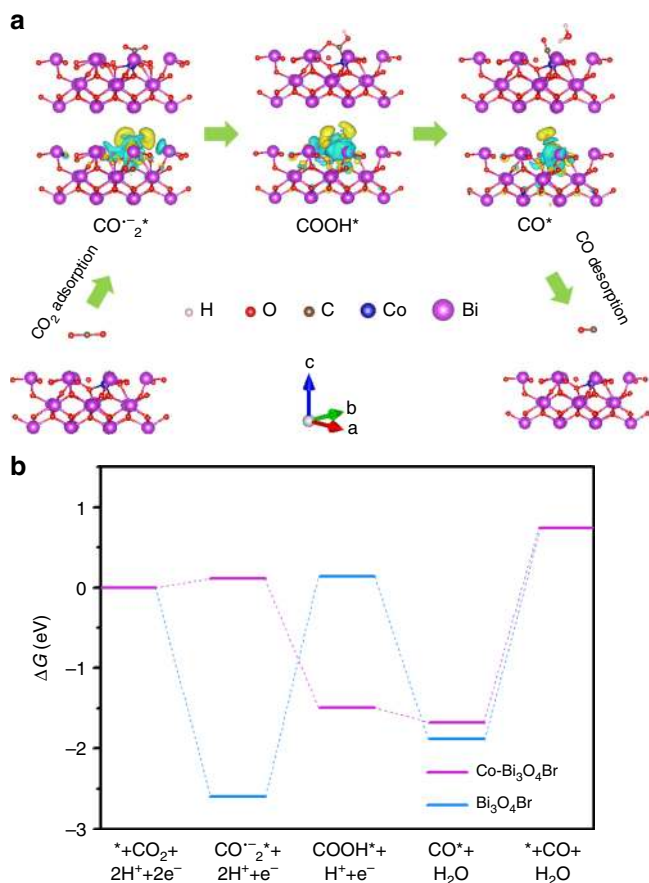


**Fig. 4** Theoretical study. **a** Schematic representation of  $\text{CO}_2$  photoreduction mechanism on the  $\text{Co-Bi}_3\text{O}_4\text{Br}$ , **b** free energy diagrams of  $\text{CO}_2$  photoreduction to  $\text{CO}$  for the  $\text{Bi}_3\text{O}_4\text{Br}$  and  $\text{Co-Bi}_3\text{O}_4\text{Br}$

the formation of adsorbed intermediate  $\text{COOH}^*$  to  $\text{CO}^*$  desorption. Our findings shed light on the rational design of metal single atom incorporated atomic layer photocatalysts for robust solar-driven  $\text{CO}_2$  conversion performances.

## Methods

**Synthesis of  $\text{Co-Bi}_3\text{O}_4\text{Br}$  atomic layer.** Totally, 0.5 mmol of  $\text{Bi}(\text{NO}_3)_3 \cdot 5\text{H}_2\text{O}$ , 0.0054 g cobalt(II) acetate tetrahydrate and 0.2 g polyvinyl pyrrolidone (PVP, K30) were dispersed into 15 mL mannitol solution (0.1 mol/L) to achieve solution A. Totally, 0.5 mmol  $\text{NaBr}$  dissolved into 3 mL mannitol solution (0.1 mol/L) to obtain solution B. Subsequently, solution B was added into solution A under stirring. After 30 min stirring,  $\text{NaOH}$  solution (2 M) was employed to tune the pH value to 11.5. Then suspension was sealed in a 25 mL teflon-lined stainless-steel autoclave and heated in oven at  $160^\circ\text{C}$  for 24 h. After cooled down, the product was gathered, washed with deionized water and ethanol for several times, and dried. The calculated Co content relative to  $\text{Bi}_3\text{O}_4\text{Br}$  is 1 wt%, and the sample is named as  $\text{Co-Bi}_3\text{O}_4\text{Br-1}$ . Adjusting the Co content to 0, 0.5, 1.5 and 2 wt% to prepare pure  $\text{Bi}_3\text{O}_4\text{Br}$ ,  $\text{Co-Bi}_3\text{O}_4\text{Br-0.5}$ ,  $\text{Co-Bi}_3\text{O}_4\text{Br-1.5}$ , and  $\text{Co-Bi}_3\text{O}_4\text{Br-2}$  samples.

**Synthesis of bulk  $\text{Bi}_3\text{O}_4\text{Br}$ .** A total of 2 mmol  $\text{Bi}_2\text{O}_3$  and 2 mmol  $\text{BiOBr}$  was sufficient mixed within 20 mL ethanol and stirred for 30 min. After drying, the powder was treated in muffle at  $650^\circ\text{C}$  for 10 h with the ramping rate of  $5^\circ\text{C min}^{-1}$  to achieve the product.

**Characterizations.** The powder X-ray diffraction (XRD) were recorded on a Shimadzu XRD-6000 X-ray diffractometer with monochromatized  $\text{Cu K}\alpha$  radiation ( $\lambda = 0.15418 \text{ nm}$ ). The XPS spectra were collected by an ESCALab MKII X-ray photoelectron spectrometer and all binding energies were calibrated by using the contaminant carbon ( $\text{C}1s = 284.6 \text{ eV}$ ) as a reference. TEM images were collected on JEOL JEM-2100F. Aberration-corrected HAADF-STEM images were collected on a Nion Ultra STEM100 (USA) operated at 100 keV in Oak Ridge National

Laboratory. Co K-edge and  $\text{Bi L}_3$ -edge X-ray absorption fine structure measurements were performed at the beamline 14W1 in Shanghai Synchrotron Radiation Facility, China. UV-vis diffuse reflection spectra of the  $\text{Bi}_3\text{O}_4\text{Br}$  and  $\text{Co-Bi}_3\text{O}_4\text{Br}$  samples were recorded on a UV-2450 UV-vis spectrophotometer (Shimadzu, Japan). The photoluminescence (PL) spectra were conducted using a Varian Cary Eclipse spectrometer (USA).  $\text{CO}_2$  adsorption measurements were carried out through TriStar II 3flex gas adsorption analyzer (Micromeritics Instrument Corporation, USA). In situ FTIR were acquired using a Bruker vertex70. All electrochemical tests were performed on a CHI 660B electrochemical system (Chenhua Instruments) in conventional three-electrode cell with Pt as the counter electrode, and  $\text{Ag/AgCl/sat. KCl}$  electrode as the reference electrode. The ultrafast TA spectra were collected by using a femtosecond laser amplifier system (Spitfire Ace, Spectra Physics), which generates laser pulses with 800 nm central wavelength and  $\sim 35 \text{ fs}$  pulse duration. The output beam was split into two beams. One was used to generate 400 nm pump light, and the other beam was focused into a sapphire plate, generating a broadband white light continuum probe beam. Both beams were focused onto the sample. After frequency resolved by a spectrograph, the excitation-induced transmission change for the probe light was collected by a home-built 46-channel synchronous digital lock-in amplifier. The isotope-labeled experiment was conducted using  $^{13}\text{CO}_2$  instead of  $^{12}\text{CO}_2$ , and the products were analyzed through gas chromatography-mass spectrometry (7890A and 5975C, Agilent).  $\text{CO}$  TPD measurements were carried out on quantachrome autosorb-iQ-C chemisorption analyzer with a thermal conductivity detector.

**Calculation details.** The first-principles simulations are conducted using the Vienna ab initio simulation package, the projector augmented wave potentials are used as pseudopotentials to describe the interactions between valence electrons and ions. The Perdew-Burke-Ernzerhof functional of generalized gradient approximation is used to describe the exchange-correlation of valence electrons. The lattice parameters of bulk  $\text{Bi}_3\text{O}_4\text{Br}$  is calculated first with the plane wave cutoff energy set as 500 eV and the k-point mesh set as  $6 \times 6 \times 2$ . The convergence criteria are  $10^{-6} \text{ eV}$  in electric relaxation energy and  $10^{-4} \text{ eV}$  in ionic relaxation energy. The optimized lattice parameter for bulk  $\text{Bi}_3\text{O}_4\text{Br}$  was  $5.78 \text{ \AA} \times 5.80 \text{ \AA} \times 19.03 \text{ \AA}$ . To calculate the  $\text{Bi}_3\text{O}_4\text{Br}$  layer slab, a  $2 \times 2 \times 1$  supercell is created and a 20 Å vacuum layer is added on top of the supercell to avoid inter-layer interactions. Thus, the lattice parameter of the layer slab model is  $11.56 \text{ \AA} \times 11.60 \text{ \AA} \times 39.03 \text{ \AA}$ , with the plane wave cutoff energy set as 500 eV and the k-point mesh set as  $3 \times 3 \times 1$ . For the case of cobalt substitution and  $\text{CO}_2$  molecule adsorption, all the parameters are remained same as that of  $\text{Bi}_3\text{O}_4\text{Br}$  layer slab, except that the convergence criteria for ionic relaxation is changed to 0.02 eV/Å instead.

**Photocatalytic  $\text{CO}_2$  reduction.** The  $\text{CO}_2$  photoreduction performance evaluation of the  $\text{Co-Bi}_3\text{O}_4\text{Br}$  samples was carried out in a 500 mL Labsolar-6A closed gas system (Perfectlight, China). Totally, 30 mg samples was added into 50 mL water and well dispersed. The system was vacuum-treated and then pumped into high-purity  $\text{CO}_2$  with pressure of 0.08 MPa. Experiments were performed at  $5^\circ\text{C}$  with a circulating water system to prevent thermal catalytic effects. The amount of  $\text{CO}$  and  $\text{CH}_4$  generated was determined using a gas chromatograph (Cotrun GC2002, FID) with a methanizer. A 300 W Xe lamp (Microsolar300, PerfectLight) was employed to provide light source. The apparent quantum efficiency is calculated according to the equation: apparent quantum efficiency =  $100\% \times (\text{number of generated } \text{CO} \times 2) / \text{number of incident photons}$ .

## Data availability

The authors declare that the data supporting the findings of this study are available within the article and the Supplementary Information files.

Received: 25 December 2018 Accepted: 29 April 2019

Published online: 28 June 2019

## References

- Zhang, L., Zhao, Z. J., Wang, T. & Gong, J. L. Nano-designed semiconductors for electro- and photoelectro-catalytic conversion of carbon dioxide. *Chem. Soc. Rev.* **47**, 5423–5443 (2018).
- Ma, Y. et al. Titanium dioxide-based nanomaterials for photocatalytic fuel generations. *Chem. Rev.* **114**, 9987–10043 (2014).
- Zhang, H. B. et al. Efficient visible-light-driven carbon dioxide reduction by a single-atom implanted metal-organic framework. *Angew. Chem. Int. Ed.* **55**, 14310–14314 (2016).
- Li, P. et al. Hexahedron prism-anchored octahedron  $\text{CeO}_2$ : crystal facet-based homojunction promoting efficient solar fuel synthesis. *J. Am. Chem. Soc.* **137**, 9547–9550 (2015).
- Long, R. et al. Isolation of Cu atoms in Pd lattice: forming highly selective sites for photocatalytic conversion of  $\text{CO}_2$  to  $\text{CH}_4$ . *J. Am. Chem. Soc.* **139**, 4486–4492 (2017).

6. Wu, J. et al. Efficient visible-light-driven CO<sub>2</sub> reduction mediated by defect-engineered BiOBr atomic layers. *Angew. Chem. Int. Ed.* **57**, 8719–8723 (2018).
7. Di, J. et al. Ultrathin two-dimensional materials for photo- and electrocatalytic hydrogen evolution. *Mater. Today* **21**, 749–770 (2018).
8. Sun, Z. Y. et al. Catalysis of carbon dioxide photoreduction on nanosheets: fundamentals and challenges. *Angew. Chem. Int. Ed.* **57**, 7610–7627 (2018).
9. Li, J., Zhan, G. M., Yu, Y. & Zhang, L. Z. Superior visible light hydrogen evolution of Janus bilayer junctions via atomic-level charge flow steering. *Nat. Commun.* **7**, 11480 (2016).
10. Yang, M. Q. et al. Self-surface charge exfoliation and electrostatically coordinated 2D hetero-layered hybrids. *Nat. Commun.* **8**, 14224 (2017).
11. Sun, Y. F., Gao, S., Lei, F. C. & Xie, Y. Atomically-thin two-dimensional sheets for understanding active sites in catalysis. *Chem. Soc. Rev.* **44**, 623–636 (2015).
12. Liang, L. et al. Infrared light-driven CO<sub>2</sub> overall splitting at room temperature. *Joule* **2**, 1–13 (2018).
13. Zhao, Y. F. et al. Defect-rich ultrathin ZnAl-layered double hydroxide nanosheets for efficient photoreduction of CO<sub>2</sub> to CO with water. *Adv. Mater.* **27**, 7824–7831 (2015).
14. Gao, S. et al. Highly efficient and exceptionally durable CO<sub>2</sub> photoreduction to methanol over freestanding defective single-unit-cell bismuth vanadate layers. *J. Am. Chem. Soc.* **139**, 3438–3445 (2017).
15. Liang, L. et al. Single unit cell bismuth tungstate layers realizing robust solar CO<sub>2</sub> reduction to methanol. *Angew. Chem. Int. Ed.* **54**, 13971–13974 (2015).
16. Jiao, X. C. et al. Defect-mediated electron-hole separation in one-unit-cell ZnIn<sub>2</sub>S<sub>4</sub> layers for boosted solar-driven CO<sub>2</sub> reduction. *J. Am. Chem. Soc.* **139**, 7586–7594 (2017).
17. Chen, Y. J. et al. Single-atom catalysts: synthetic strategies and electrochemical applications. *Joule* **2**, 1242–1264 (2018).
18. Wang, A. Q., Li, J. & Zhang, T. Heterogeneous single-atom catalysis. *Nat. Rev. Chem.* **2**, 65–81 (2018).
19. Wang, X. Q. et al. Regulation of coordination number over single Co sites: triggering the efficient electroreduction of CO<sub>2</sub>. *Angew. Chem. Int. Ed.* **57**, 1944–1948 (2018).
20. Pan, Y. et al. Design of single-atom Co-N<sub>5</sub> catalytic site: a robust electrocatalyst for CO<sub>2</sub> reduction with nearly 100% CO selectivity and remarkable stability. *J. Am. Chem. Soc.* **140**, 4218–4221 (2018).
21. Zhou, J. D. et al. A library of atomically thin metal chalcogenides. *Nature* **556**, 355–359 (2018).
22. Gao, C. et al. Heterogeneous single-atom catalyst for visible-light-driven high-turnover CO<sub>2</sub> reduction: the role of electron transfer. *Adv. Mater.* **30**, 1704624 (2018).
23. Li, H. et al. Oxygen vacancy structure associated photocatalytic water oxidation of BiOCl. *ACS Catal.* **6**, 8276–8285 (2016).
24. Di, J., Xiong, J., Li, H. M. & Liu, Z. Ultrathin 2D photocatalysts: electronic-structure tailoring, hybridization, and applications. *Adv. Mater.* **30**, 1704548 (2018).
25. Lei, F. C. et al. Atomic-layer-confined doping for atomic-level insights into visible-light water splitting. *Angew. Chem. Int. Ed.* **54**, 9266–9270 (2015).
26. Liu, W. et al. Single-site active cobalt-based photocatalyst with a long carrier lifetime for spontaneous overall water splitting. *Angew. Chem. Int. Ed.* **56**, 9312–9317 (2017).
27. Li, X. G. et al. Single-atom Pt as co-catalyst for enhanced photocatalytic H<sub>2</sub> evolution. *Adv. Mater.* **28**, 2427–2431 (2016).
28. Jiao, X. C. et al. Partially oxidized SnS<sub>2</sub> atomic layers achieving efficient visible-light-driven CO<sub>2</sub> reduction. *J. Am. Chem. Soc.* **139**, 18044–18051 (2017).
29. Di, J. et al. Defect-rich Bi<sub>12</sub>O<sub>17</sub>Cl<sub>2</sub> nanotubes self-accelerating charge separation for boosting photocatalytic CO<sub>2</sub> reduction. *Angew. Chem. Int. Ed.* **57**, 14847–14851 (2018).
30. Chang, X. X., Wang, T. & Gong, J. L. CO<sub>2</sub> photo-reduction: insights into CO<sub>2</sub> activation and reaction on surfaces of photocatalysts. *Energy Environ. Sci.* **9**, 2177–2196 (2016).

## Acknowledgements

This work was financially supported by MOE Tier 1 grant RG4/17, MOE Tier 2 grant MOE2016-T2-1-131, and Singapore National Research Foundation under NRF award number NRF-NRFF2013-08. This work also supported by the National Natural Science Foundation of China (Nos. 21676128, 21606113, and 21576123). S.Z.Y. was supported by the U.S. Department of Energy, Office of Science, Basic Energy Sciences, Materials Science and Engineering Division and through a user project supported by ORNL's Center for Nanophase Materials Sciences.

## Author contributions

J.D., J.X.X., and Z.L. conceived and designed the experiments. J.D. prepared and characterized the photocatalysts and performed the photocatalytic experiments. S.Z.Y. and C.Z. carried out STEM. C.C., W.H., and S.Z.L. provided theoretical calculation and discussion. L.S. and S.M.C. analyzed the EXAFS data. M.L.D. and R.L. carried out the isotope-labeled experiment. Z.C., H.L.C., and Y.X.W. carried out the TA spectra. J.X. and H.M.L. discussed the results and commented on the paper. J.D. wrote the paper, J.X.X. and Z.L. revised the paper.

## Additional information

**Supplementary Information** accompanies this paper at <https://doi.org/10.1038/s41467-019-10392-w>.

**Competing interests:** The authors declare no competing interests.

**Reprints and permission** information is available online at <http://npg.nature.com/reprintsandpermissions/>

**Peer Review Information:** *Nature Communications* thanks Linqun Ye and the other anonymous reviewer(s) for their contribution to the peer review of this work.

**Publisher's note:** Springer Nature remains neutral with regard to jurisdictional claims in published maps and institutional affiliations.



**Open Access** This article is licensed under a Creative Commons Attribution 4.0 International License, which permits use, sharing, adaptation, distribution and reproduction in any medium or format, as long as you give appropriate credit to the original author(s) and the source, provide a link to the Creative Commons license, and indicate if changes were made. The images or other third party material in this article are included in the article's Creative Commons license, unless indicated otherwise in a credit line to the material. If material is not included in the article's Creative Commons license and your intended use is not permitted by statutory regulation or exceeds the permitted use, you will need to obtain permission directly from the copyright holder. To view a copy of this license, visit <http://creativecommons.org/licenses/by/4.0/>.

© The Author(s) 2019